ISM Properties of a Massive Dusty Star-forming Galaxy Discovered at $z \sim 7$

M. L. Strandet[1,2], A. Weiss[1], C. De Breuck[3], D. P. Marrone[4], J. D. Vieira[5,6], M. Aravena[7], M. L. N. Ashby[8], M. Béthermin[9], M. S. Bothwell[10,11], C. M. Bradford[12], J. E. Carlstrom[13,14,15,16], S. C. Chapman[17], D. J. M. Cunningham[17,18], Chian-Chou Chen[3], C. D. Fassnacht[19], A. H. Gonzalez[20], T. R. Greve[21], B. Gullberg[22], C. C. Hayward[8,23], Y. Hezaveh[24,27], K. Litke[4], J. Ma[20], M. Malkan[25], K. M. Menten[1], T. Miller[17], E. J. Murphy[26], D. Narayanan[20], K. A. Phadke[5], K. M. Rotermund[17], J. S. Spilker[4], and J. Sreevani[5]

[1] Max-Planck-Institut für Radioastronomie, Auf dem Hügel 69, D-53121 Bonn, Germany
[2] Member of the International Max Planck Research School (IMPRS) for Astronomy and Astrophysics at the Universities of Bonn and Cologne, D-53121 Bonn, Germany
[3] European Southern Observatory, Karl Schwarzschild Straße 2, D-85748 Garching, Germany
[4] Steward Observatory, University of Arizona, 933 North Cherry Avenue, Tucson, AZ 85721, USA
[5] Department of Astronomy, University of Illinois, 1002 West Green Street, Urbana, IL 61801, USA
[6] Department of Physics, University of Illinois, 1002 West Green Street, Urbana, IL 61801, USA
[7] Núcleo de Astronomía, Facultad de Ingeniería y Ciencias, Universidad Diego Portales, Av. Ejército 441, Santiago, Chile
[8] Harvard-Smithsonian Center for Astrophysics, 60 Garden Street, Cambridge, MA 02138, USA
[9] Aix Marseille Univ., CNRS, LAM, Laboratoire d'Astrophysique de Marseille, Marseille, France
[10] Cavendish Laboratory, University of Cambridge, 19 J.J. Thomson Avenue, Cambridge CB3 0HE, UK
[11] Kavli Institute for Cosmology, University of Cambridge, Madingley Road, Cambridge CB3 0HA, UK
[12] Jet Propulsion Laboratory, 4800 Oak Grove Drive, Pasadena, CA 91109, USA
[13] Kavli Institute for Cosmological Physics, University of Chicago, 5640 South Ellis Avenue, Chicago, IL 60637, USA
[14] Department of Physics, University of Chicago, 5640 South Ellis Avenue, Chicago, IL 60637, USA
[15] Enrico Fermi Institute, University of Chicago, 5640 South Ellis Avenue, Chicago, IL 60637, USA
[16] Department of Astronomy and Astrophysics, University of Chicago, 5640 South Ellis Avenue, Chicago, IL 60637, USA
[17] Dalhousie University, Halifax, Nova Scotia, Canada
[18] Department of Astronomy and Physics, Saint Mary's University, Halifax, Nova Scotia, Canada
[19] Department of Physics, University of California, One Shields Avenue, Davis, CA 95616, USA
[20] Department of Astronomy, University of Florida, Bryant Space Sciences Center, Gainesville, FL 32611 USA
[21] Department of Physics and Astronomy, University College London, Gower Street, London WC1E 6BT, UK
[22] Centre for Extragalactic Astronomy, Department of Physics, Durham University, South Road, Durham DH1 3LE, UK
[23] Center for Computational Astrophysics, Flatiron Institute, 162 Fifth Avenue, New York, NY 10010, USA
[24] Kavli Institute for Particle Astrophysics and Cosmology, Stanford University, Stanford, CA 94305, USA
[25] Department of Physics and Astronomy, University of California, Los Angeles, CA 90095-1547, USA
[26] National Radio Astronomy Observatory, 520 Edgemont Road, Charlottesville, VA 22903, USA

Abstract

We report the discovery and constrain the physical conditions of the interstellar medium of the highest-redshift millimeter-selected dusty star-forming galaxy to date, SPT-S J031132−5823.4 (hereafter SPT0311−58), at $z = 6.900 \pm 0.002$. SPT0311−58 was discovered via its 1.4 mm thermal dust continuum emission in the South Pole Telescope (SPT)-SZ survey. The spectroscopic redshift was determined through an Atacama Large Millimeter/submillimeter Array 3 mm frequency scan that detected CO(6–5), CO(7–6), and [C I](2–1), and subsequently was confirmed by detections of CO(3–2) with the Australia Telescope Compact Array and [C II] with APEX. We constrain the properties of the ISM in SPT0311−58 with a radiative transfer analysis of the dust continuum photometry and the CO and [C I] line emission. This allows us to determine the gas content without ad hoc assumptions about gas mass scaling factors. SPT0311−58 is extremely massive, with an intrinsic gas mass of $M_{\mathrm{gas}} = 3.3 \pm 1.9 \times 10^{11} M_{\odot}$. Its large mass and intense star formation is very rare for a source well into the epoch of reionization.

Key words: early universe – galaxies: high-redshift – galaxies: star formation

1. Introduction

Searches for the most distant galaxies have now reached as far back as the first billion years in the history of the universe and are peeking into the epoch of reionization (EoR) at $6 < z < 11$ (Planck Collaboration et al. 2016). Some of the most important questions in observational cosmology concern the timescale over which the reionization of the universe took place, the identification of the objects providing the ionizing photons and the enrichment of galaxies with metals. It is expected that star-forming galaxies play a major role in the reionization, so to understand the evolution of the universe from its neutral

beginning to its present ionized state we must study the galaxies in the EoR (see reviews by Bouwens 2016; Stark 2016). How galaxies formed and evolved in the EoR is unknown. Galaxies in this era are currently being found from rest-frame ultraviolet (UV) surveys (e.g., Ouchi et al. 2010). Most of these systems, however, are low-mass star-forming galaxies for which the enrichment of the cold ISM is difficult to study even in long integrations with the Atacama Large Millimeter/submillimeter Array (ALMA; Bouwens et al. 2016).

Massive dusty star-forming galaxies (DSFGs; Casey et al. 2014) are not expected to be found into the EoR because it is difficult to produce their large dust masses within a few hundred Myr of the Big Bang (Ferrara 2010; Mattsson 2015). Recent wide-area
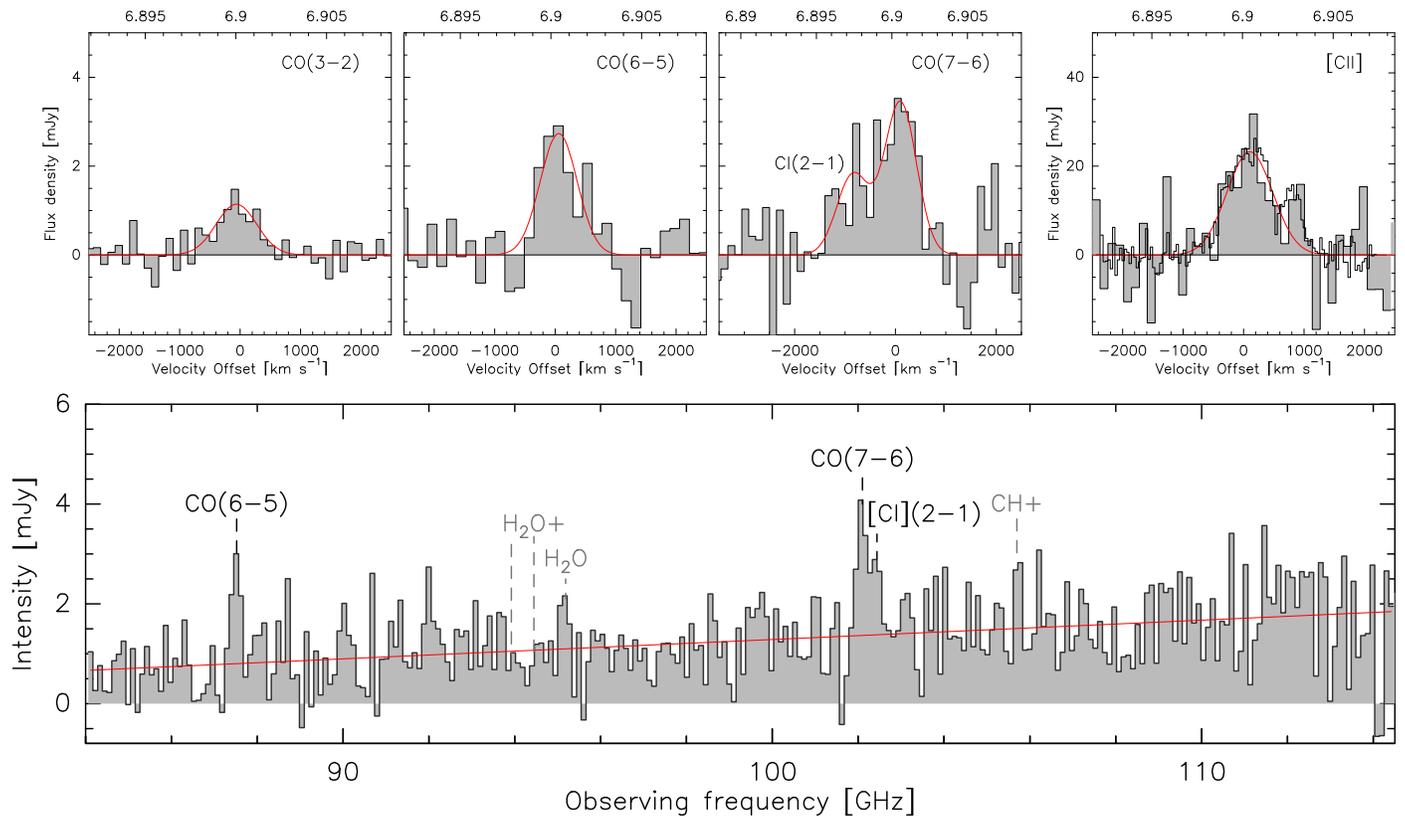
---

[27] Hubble Fellow.

Figure 1. The lower part of the figure shows the ALMA 3 mm spectrum of SPT0311−58 spanning 84.2–114.9 GHz. The spectrum has been binned to best show the lines. Transitions labeled in black are detected, and gray labels indicate where other transitions should be. The red line indicates the zeroth-order baseline. The sub-panels above the spectrum show, from left to right, the continuum-subtracted spectra of ATCA CO(3–2), ALMA CO(6–5), ALMA CO(7–6) and C I (2–1), and APEX [C II] with ALMA [C II] overlaid as a solid black histogram. Gaussian fits to the spectra are shown in red.

Herschel and optical QSO surveys, however, have revealed dusty galaxies out to $z \sim 6$–7 (e.g., Venemans et al. 2012; Riechers et al. 2013). These systems offer the unique opportunity to study extreme cases of metal/dust enrichment of the ISM within the EoR in the most massive overdensities at these redshifts.

Here, we present the DSFG SPT-S J031132−5823.4 (hereafter SPT0311−58) discovered in the South Pole Telescope (SPT)-SZ survey (Carlstrom et al. 2011; Vieira et al. 2013). SPT0311−58 is the highest-redshift millimeter-selected DSFG known to date, located well into the EoR at a redshift of $z = 6.900 \pm 0.002$. With this source, we take a step of almost 100 Myr closer to the Big Bang than the previously most distant DSFG at $z = 6.34$ found by Riechers et al. (2013), bringing us ∼760 Myr away from Big Bang. Throughout the paper, we assume a ΛCDM cosmology with $H_0 = 70$ km s^{-1} Mpc^{-1}, $\Omega_\Lambda = 0.7$, and $\Omega_M = 0.3$.

2. Observational Results

2.1. Determining the Redshift

The redshift search for SPT0311-58 was performed in ALMA band 3 by combining five tunings covering 84.2–114.9 GHz (project ID: 2015.1.00504.S; see Weiß et al. 2013; Strandet et al. 2016 for further details on the observing setup). The observations were carried out on 2015 December 28 and 2016 January 2 in the Cycle 3 compact array configuration. The number of antennas varied from 34 to 41, with baselines up to 300 m yielding a synthesized beam size of $2\rlap{.}''2$–$3\rlap{.}''0$. Typical system temperatures for the observations

were $T_{sys} = 50$–80 K (SSB). Flux calibration was done with Uranus, bandpass calibration with J0334−4008, and phase calibration with J0303−6211 and J0309−6058. The on-source time varied between 60 and 91 s per tuning, accounting for a total of 6 minutes and 10 s. The data were processed using the Common Astronomy Software Application package (McMullin et al. 2007).

We created a cleaned 3 mm continuum image combining all five tunings. This yields a high signal-to-noise ratio (S/N) detection of ∼35. We also generated a spectral cube using natural weighting with a channel width of 19.5 MHz (50–65 km s^{-1} for the highest and lowest observing frequency, respectively), which gives a typical noise per channel of 0.9–1.7 mJy beam^{-1}.

The ALMA 3 mm spectrum of SPT0311−58 was extracted at the centroid of the 3 mm continuum emission (α: $03^h11^m33\rlap{.}^s142$ δ: $-58°23'33\rlap{.}''37$ (J2000)) and is shown in Figure 1. We detect emission in the CO $J = 6$–5 and 7–6 lines and the [C I]$^3P_2 - ^3P_1$ line (in the following 2–1) and their noise-weighted line frequencies yield a redshift of $z = 6.900 \pm 0.002$. We also see hints of H$_2$O(2_{11}–2_{02}) and CH$^+$(1–0), but these are not formally detected in this short integration.

The line and continuum properties are given in Table 1. For the fit to the CO(7–6) and [C I](2–1) lines we fix the line width to the mean value derived from the unblended lines. Their uncertainties include the variations of the line intensities for a fit where the line width is a free parameter.

Table 1
Observed Properties of SPT0311-58

	Line Properties				Continuum Properties	
Transition	$\int SdV$ (Jy km s^{-1})	dV[a] (km s^{-1})	L' $\times 10^{11}$ (K km s^{-1} pc^{-2})	L $\times 10^8$ ($L_\odot$)	Wavelength (μm)	S_ν (mJy)
CO(3–2)	0.96 ± 0.15	790 ± 150	1.52 ± 0.24	2.01 ± 0.32	3000	1.30 ± 0.05
CO(6–5)	2.10 ± 0.33	720 ± 140	0.83 ± 0.13	8.8 ± 1.4	2000	7.5 ± 1.3
CO(7–6)	2.78 ± 0.80	750[b]	0.81 ± 0.11	13.6 ± 1.8	1400	19.0 ± 4.2
[C I](2–1)	1.29 ± 0.80	750[b]	0.37 ± 0.10	6.4 ± 1.8	870	32.0 ± 5.0
[C II]$_{\rm APEX}$	22.1 ± 5.1	890 ± 260	1.16 ± 0.27	254 ± 59	500	52.0 ± 8.0
[C II]$_{\rm ALMA}$	25.88 ± 0.65		1.36 ± 0.03	298.1 ± 7.5	350	38.0 ± 6.0
					250	29.0 ± 8.0

Notes.
[a] FWHM.
[b] Fixed from CO(3–2) and CO(6–5).

2.2. Observations of CO(3–2) and [CII]

We used the 7 mm receivers of the Australia Telescope Compact Array (ATCA) to observe the CO(3–2) line (project ID: CX352). Observations were carried out with the hybrid H214 array, which yields a beam size of 5″–6″ at the observing frequency of 43.77 GHz. The line is detected with an S/N of 5.0 at a frequency and line width consistent with the ALMA derived redshift and line profiles.

In addition, we used the Atacama Pathfinder Experiment (APEX) to observe [C II] at 240.57 GHz. The observations were carried out in 2016 April–May in good weather conditions with a precipitable water vapor content <1.5 mm (project IDs: E-296.A-5041B-2016 and M-097.F-0019-2016). The observations were performed and the data processed as described by Gullberg et al. (2015). The [C II] line is detected with an S/N of 4.3. From ALMA high spatial resolution observations of the [C II] line (D. P. Marrone et al. 2017, in preparation; project ID: 2016.1.01293.S), we extract a [C II] spectrum and flux, which are in good agreement with the APEX data. We adopt the ALMA [C II] flux hereafter.

The line parameters derived from Gaussian fits to the data are given for both transitions in Table 1; the spectra are shown in Figure 1.

2.3. FIR Dust Continuum

Table 1 (right) summarizes the dust continuum observations of SPT0311−58. With seven broadband continuum detections between 3 mm to 250 μm, the far-infrared spectral energy distribution (SED) of SPT0311−58 is thoroughly covered.

The SPT 1.4 and 2.0 mm flux densities were extracted and deboosted as described by Mocanu et al. (2013). We obtained a 870 μm map with APEX/LABOCA (project ID: M-091.F-0031-2013). The data were obtained and reduced, and the flux was extracted following Greve et al. (2012). Using *Herschel*/SPIRE, we obtained maps at 250, 350, and 500 μm (project ID: DDT_mstrande_1). The data were obtained and reduced as described by Strandet et al. (2016).

From our photometry, we derive an apparent far-infrared (FIR) luminosity (integrated between 40 and 120 μm rest) of $L_{\rm FIR} = 4.1 \pm 0.7 \times 10^{13}\ L_\odot$ (see Figure 2).

3. Characterizing the ISM in SPT0311−58

3.1. Source Properties from High-resolution Imaging

ALMA high spatial resolution imaging (angular resolution of $0.3 \times 0.''5$) of the [C II] line in SPT0311−58 shows that the system consists of two galaxies in close proximity (D. P. Marrone et al. 2017, in preparation). Only the western source is significantly gravitationally magnified, and this source dominates the apparent continuum luminosity (>90% of the rest-frame 160 μm continuum flux density is emitted by the western source). In the following, we assume that the contribution from the eastern source is negligible and models the system as a single object, using the system magnification of $\mu = 1.9$ (D. P. Marrone et al. 2017, in preparation).

3.2. Radiative Transfer Models

We use the FIR photometry and the line luminosities from Table 1 to simultaneously model the dust continuum, CO spectral line energy distribution (SLED), and the [C I](2−1) line following the radiative transfer calculation presented in Weiß et al. (2007). In this model, the background radiation field is set to the cosmic microwave background (CMB) for the dust and to the CMB plus the dust radiation field for the lines. The line and dust continuum emission are further linked via the gas column density in each component that introduces the turbulence line width as a free parameter in the calculation (see Equation (7) in Weiß et al. 2007). The gas column density calculated from the line emission together with the gas-to-dust-mass ratio (GDMR) then determines the optical depth of the dust.

The calculations treat the dust and the kinetic temperature as independent parameters, but with the prior that the kinetic gas temperature has to be equal to or higher than the dust temperature. Physically, this allows for additional sources of mechanical energy (e.g., shocks) in the ISM in addition to photo-electric heating.

The chemical parameters in our model are the CO and [C I] abundances relative to H_2 and the GDMR. We use a fixed CO abundance of 8×10^{-5} relative to H_2 (Frerking et al. 1982), but keep the [C I] abundance and the GDMR as free parameters. For the frequency dependence of the dust absorption coefficient we adopt $\kappa_{\rm d}(\nu) = 0.04(\nu/250\ {\rm GHz})^\beta$ [m^2 kg^{-1}] (Krügel & Siebenmorgen 1994), which is in good
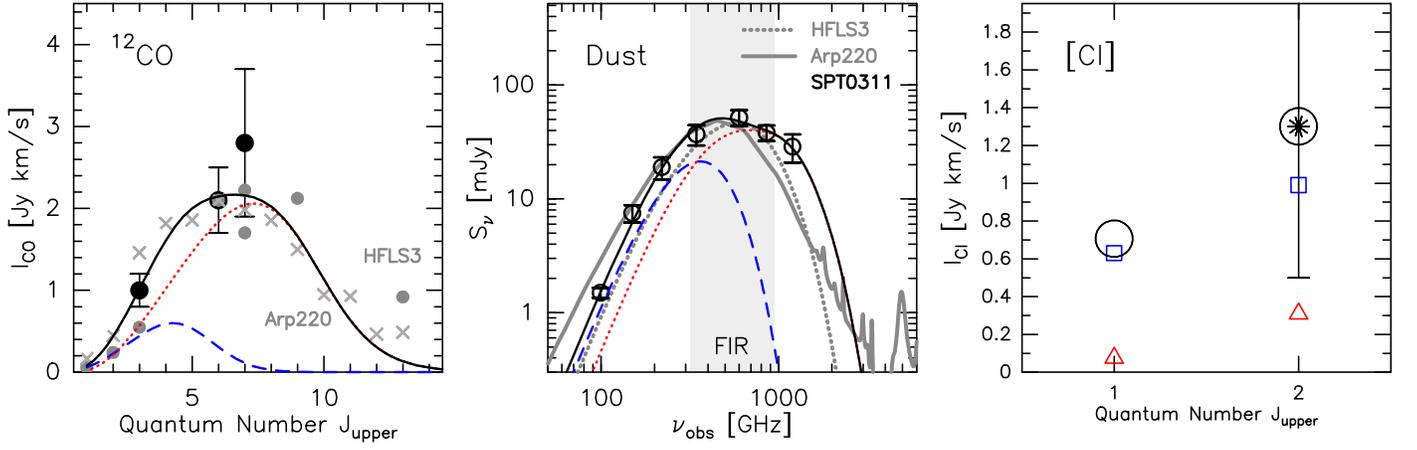
Figure 2. Results of simultaneous fitting of the CO-SLED (left), SED (middle), and [C I] (right) line flux. The CO line intensities are plotted as filled circles, the continuum fluxes as open circles and the [C I] flux as an asterisk. The blue dashed line and squares show the cold component, the red dotted line and triangles show the warm component, the black solid line and circles (in the right panel) show the combination of the two components. In gray is shown similar data for HFLS3 (dots and dotted line) and Arp220 (crosses and solid line), normalized to the CO(6–5) flux of SPT0311-58 for the CO-SLED and to the peak of the continuum SED of SPT0311-58 for the SED. The line fluxes and continuum properties fitted are listed in Table 2. Left: two-component CO-SLED. Middle: two-component SED fitting based. Right: the contribution of each of the two components to the [C I](2–1) line and predictions for the [C I](1–0) line.

Table 2
ISM Parameters of SPT0311-58 from the Radiative Transfer Calculation

Parameter	Unit	Overall	Cold Component	Warm Component
Equivalent radius[a]	pc	$(4000 \pm 1700)\mu^{-1/2}$	$(3700 \pm 1300)\mu^{-1/2}$	$(1500 \pm 1200)\mu^{-1/2}$
T_{dust}	K		36 ± 7	115 ± 54
T_{kin}	K		58 ± 23	180 ± 51
$\log(n(H_2))$	cm^{-3}		3.7 ± 0.4	5.1 ± 1.9
dv_{turb}	$km\ s^{-1}$		130 ± 17	100 ± 4
κ_{vir}[b]			1.9 ± 1.9	3.1 ± 2.5
GDMR			110 ± 15[d]	
β			1.91 ± 0.05[d]	
[C I]/[H_2]			$(6.0 \pm 1.4) \times 10^{-5}$	$(1.7 \pm 2.3) \times 10^{-5}$
M_{dust}	$M_\odot$	$(5.7 \pm 0.8) \times 10^9\ \mu^{-1}$	$(5.2 \pm 0.7) \times 10^9\ \mu^{-1}$	$(4.8 \pm 0.7) \times 10^8\ \mu^{-1}$
M_{gas}	$M_\odot$	$(6.3 \pm 3.7) \times 10^{11}\ \mu^{-1}$	$(5.7 \pm 3.8) \times 10^{11}\ \mu^{-1}$	$(5.3 \pm 3.8) \times 10^{10}\ \mu^{-1}$
α_{CO}	$M_\odot/K\ km\ s^{-1}\ pc^2$	4.8 ± 2.9	5.5 ± 4.0	3.1 ± 2.5
L_{FIR}	$L_\odot$	$(4.1 \pm 0.7) \times 10^{13}\ \mu^{-1}$	$(1.2 \pm 1.1) \times 10^{13}\ \mu^{-1}$	$(2.9 \pm 0.7) \times 10^{13}\ \mu^{-1}$
SFR[c]	$M_\odot\ yr^{-1}$	$(4100 \pm 700)\mu^{-1}$		
t_{dep}	Myr	150 ± 90		

Notes. The values here are apparent values. Intrinsic values can be calculated using $\mu = 1.9$.
[a] $r_0 = D_A\ \sqrt{\Omega_s/\pi}$.
[b] $dv/dr = \kappa_{vir} \times 3.1\sqrt{n(H_2)/1e4}$; we calculate the velocity gradient for virialized clouds ($\kappa_{vir} = 1$; Goldsmith 2001) but also consider nonvirial, unbound motions ($\kappa_{vir} > 1$; Greve et al. 2009).
[c] Using SFR $= 10^{-10} \times L_{FIR}$ based on a Chabrier initial mass function (Kennicutt 1998; Chabrier 2003).
[d] Fitted in the radiative transfer calculation but set to be the same for both components.

agreement with $\kappa_{870\,\mu m} = 0.077\ m^2\ kg^{-1}$ used in other work (see Spilker et al. 2015 and references therein), for our best-fitting β.

Model solutions are calculated employing a Monte Carlo Bees (Pham & Castellani 2009) algorithm that randomly samples the parameter space and gives finer sampling for good solutions (as evaluated from a χ^2 analysis for each model). In total, we sample $\sim 10^7$ models. Parameter values and uncertainties were calculated using the probability-weighted mean of all solutions and the standard deviations.

3.3. Model Results

Figure 2 shows the CO-SLED, the continuum SED, and [C I] flux density. From the figure, it is apparent that the dust continuum SED cannot be modeled with a single-temperature modified blackbody, so we instead fit two components. Since we have no information on the high-J CO transition, we use the shape of the CO-SLED of Arp220 (Rosenberg et al. 2015) and HFLS3 (Riechers et al. 2013) as priors. With this choice, we compare the moderately excited CO-SLED of Arp220 (see Rosenberg et al. (2015) for a comparison of Arp220 to other

local ULIRGs) to the more extreme case of HFLS3 where the CO-SLED stays high up to the $J_{up} = 9$ level (see Figure 2). The use of the priors mainly affects the parameters of the warm gas and therefore only has a small effect on our derived gas mass (see below). Table 2 lists the parameters obtained from the radiative transfer calculations for the Arp220 prior, not corrected for magnification.

For both priors, the warm dust component dominates the peak of the CO-SLED and the short-wavelength part of the dust spectrum and therefore the FIR luminosity. Its size is small compared to the cold gas with an area ratio of ~ 6 ($r_0 = 1.7 \pm 1.4$ kpc where r_0 is the equivalent radius defined as $r_0 = D_A \sqrt{\Omega_s/\pi}$; Weiß et al. 2007; for HFLS3 and slightly smaller for Arp220), which implies that the region of intense FIR continuum emission is significantly smaller than the overall gas distribution. Due to a lack of observations of CO transitions beyond (7–6), its properties are mainly driven by the assumed shape of the CO-SLED for the high-J transitions. However, the models for both priors indicated consistently that the warm gas has a substantial density (of the order of 10^5 cm^{-3}), a dust temperature of ~ 100 K, and a kinetic temperature in excess (but consistent within the errors) of the dust temperature ($T_{kin} = 180 \pm 50$ K when using Arp220 priors).

The cold dust component is required to fit the CO(3–2) and [C I] line emission and the long-wavelength part of the dust SED. Due to its large extent and relatively high density ($r_0 = 3.7 \pm 1.3$ kpc, $\log(n(H_2) = 3.7 \pm 0.4)$), it carries $\approx 90\%$ of the gas mass. The abundance of neutral carbon in this gas phase is $[C I]/[H_2] = 6.0 \pm 1.4 \times 10^{-5}$, in agreement with other estimates at high redshift and in nearby galaxies (e.g., Weiß et al. 2005 and references therein). For both priors, the cold gas dominates the CO(1–0) line luminosity. As for the warm gas, we find that the kinetic temperature is above the dust temperature ($T_{dust} = 36 \pm 7$ K, $T_{kin} = 58 \pm 23$ K), which may suggest that the ISM in SPT0311-58 experiences additional mechanical energy input, e.g., via feedback from stellar winds or AGN driven outflows. This is also supported by the large turbulent line width of order 100 km s^{-1} and super-virial velocity gradients ($\kappa_{vir} > 1$; see footnote b in Table 2) that we find for both components and priors.

We use the kinematic parameters (dv_{turb} and κ_{vir}) together with the source size and the H_2 density for each component (see Equation (8) in Weiß et al. 2007) to derive a total apparent gas mass of $M_{gas} = (6.3 \pm 3.7) \times 10^{11} M_\odot$ (including a 36% correction to account for the cosmic He abundance). For the HFLS3 prior, the gas mass is $\sim 30\%$ higher.

4. Discussion

4.1. Gas Mass Conversion Factor

With the independent gas mass estimate from the radiative transfer models in hand we can also derive the GDMR and the CO-to-H_2 conversion factor (α_{CO}) for SPT0311-58. Since the CO(1–0) transition has not been observed, we use the flux density from the radiative transfer model that predicts $I_{CO(1-0)} = 0.10 \pm 0.03$ Jy km s^{-1}. In our models, we assume that each gas component has the same GDMR, and we find GDMR $= 110 \pm 15$. Due to the different physical conditions in each gas component, there is a specific α_{CO} value for each component. For the cold dust component, we find $\alpha_{CO} = 5.5 \pm 4.0$ $M_\odot$(K km s^{-1} pc^2)$^{-1}$, and for the warm dust

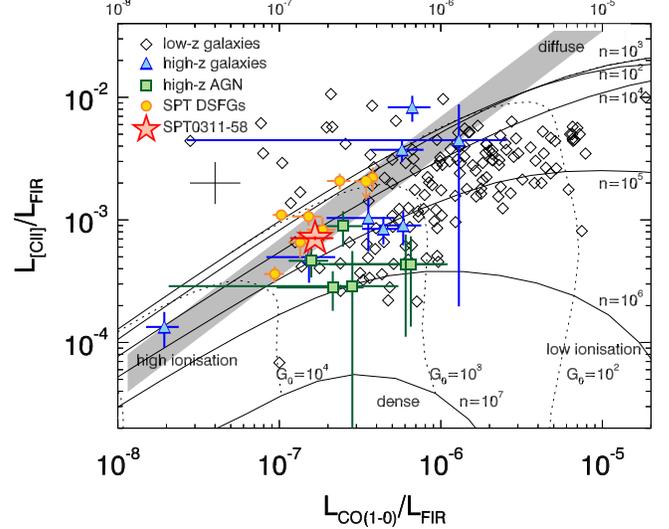**Figure 3.** $L_{[C II]}/L_{FIR}$ vs. $L_{[C II]}/L_{CO(1-0)}$ with PDR models and samples adapted from Gullberg et al. (2015). The red star shows how SPT0311-58 falls within the larger SPT DSFG sample. The typical error bar for the low-redshift sample is presented by the black cross.

component, $\alpha_{CO} = 3.1 \pm 2.5$ $M_\odot$(K km s^{-1} pc^2)$^{-1}$. Combining both gas components we find for SPT0311-58 $\alpha_{CO} = 4.8 \pm 2.9$ $M_\odot$(K km s^{-1} pc^2)$^{-1}$.

When calculating gas masses for ULIRGs, a factor of $\alpha_{CO} = 0.8$ $M_\odot$(K km s^{-1} pc^2)$^{-1}$ is typically assumed (Downes & Solomon 1998), significantly below our estimate. The difference can easily be explained by the much higher densities we find in both components compared to the models from Downes & Solomon (1998), in which most of the CO(1–0) luminosity arises from a diffuse inter-cloud medium. Since the bulk of the gas mass of this source is in the dense component, it is vital to include the higher-J CO transitions in the calculation of α_{CO}.

A similar two-component analysis was done for the broad absorption line quasar APM08279+5255 at $z = 3.9$ (Weiß et al. 2007), where the dense component was found to dominate the CO(1–0) line by 70%. They find a high conversion factor of $\alpha_{CO} \sim 6$ $M_\odot$(K km s^{-1} pc^2)$^{-1}$, similar to what we find in the dense gas component. A similar reasoning for higher CO conversion factors owing to the presence of dense gas was put forward by Papadopoulos et al. (2012) based on the CO-SLED in local (U)LIRGs.

4.2. [CII]

From our [C II] detection, we derive a $L_{[C II]}/L_{FIR}$ ratio of $(7.3 \pm 0.1) \times 10^{-4}$. Figure 3 shows that this puts SPT0311-58 into the lower region of the $L_{[C II]}/L_{FIR}$ ratio observed in a larger sample of SPT-DSFGs (Gullberg et al. 2015). Similarly, low $L_{[C II]}/L_{FIR}$ ratios are found for the $z = 6.3$ star-forming galaxy HFLS3 (Riechers et al. 2013) and for the $z = 7.1$ QSO host galaxy J1120+0641 (Venemans et al. 2012).

The $L_{[C II]}/L_{CO(1-0)}$ ratio in SPT0311-58 is similar to what is observed in the SPT sample (4300 ± 1300 compared to 5200 ± 1800; Gullberg et al. 2015) and HFLS3 (~ 3000; Riechers et al. 2013). This is consistent with the picture in which the [C II] emission stems from the surface of dense clouds exposed to the strong UV field from the intense starburst

in SPT0311−58 (Stacey et al. 2010; Gullberg et al. 2015; Spilker et al. 2016).

The larger [C II] deficit together with the decreasing $L_{[C II]}/L_{CO(1-0)}$ ratio of SPT0311−58 and other high-redshift sources compared to local galaxies may be understood as a consequence of an increasing gas surface density (Narayanan & Krumholz 2017): the higher molecular gas surface density pushes the $H_I + H_2$ mass budget toward higher H_2 fractions. Since [C II] mainly arises from the PDR zone associated with H_I and the outer H_2 layer, this effect reduces the size of the [C II] emitting region and therefore the [C II] line intensity. At the same time, the ratio of $L_{[C II]}/L_{CO(1-0)}$ will decrease due to an increase in the fraction of carbon locked in CO compared to [C II].

4.3. Concluding Remarks

Both our radiative transfer model and fine structure line results indicate that SPT0311-58 resembles typical DSFGs, just at $z \sim 7$. This is also supported by its extreme SFR surface density of $\Sigma_{SFR} \sim 600 \, M_\odot \, yr^{-1} \, kpc^{-2}$ (derived using the size of the warm gas component that dominates the FIR luminosity), which approaches the modeled values for radiation pressure limited starbursts ($10^3 \, M_\odot \, yr^{-1} kpc^{-2}$; Thompson et al. 2005) and is comparable to what is found in other starbursts like Arp220, HFLS3, and other SPT-DSFGs (Scoville 2003; Riechers et al. 2013; Spilker et al. 2016). Future observations of this source will explore its spatial structure, physical conditions, formation history, and chemical evolution in great detail as it is one of very few massive galaxies known at $z \sim 7$.

References

Bouwens, R. 2016, in Understanding the Epoch of Cosmic Reionization, Astrophysics and Space Science Library, Vol. 423, ed. A. Mesinger (Cham: Springer International), 111

Bouwens, R. J., Aravena, M., Decarli, R., et al. 2016, ApJ, 833, 72

Carlstrom, J. E., Ade, P. A. R., Aird, K. A., et al. 2011, PASP, 123, 568

Casey, C. M., Narayanan, D., & Cooray, A. 2014, PhR, 541, 45

Chabrier, G. 2003, ApJL, 586, L133

Downes, D., & Solomon, P. M. 1998, ApJ, 507, 615

Ferrara, A. 2010, in AIP Conf. Ser. 1294, The First Stars and Galaxies: Challenges for the Next Decade, ed. D. J. Whalen, V. Bromm, & N. Yoshida (Melville, NY: AIP), 148

Frerking, M. A., Langer, W. D., & Wilson, R. W. 1982, ApJ, 262, 590

Goldsmith, P. F. 2001, ApJ, 557, 736

Greve, T. R., Papadopoulos, P. P., Gao, Y., & Radford, S. J. E. 2009, ApJ, 692, 1432

Greve, T. R., Vieira, J. D., Weiß, A., et al. 2012, ApJ, 756, 101

Gullberg, B., De Breuck, C., Vieira, J. D., et al. 2015, MNRAS, 449, 2883

Kennicutt, R. C., Jr. 1998, ApJ, 498, 541

Krügel, E., & Siebenmorgen, R. 1994, A&A, 288, 929

Mattsson, L. 2015, arXiv:1505.04758

McMullin, J. P., Waters, B., Schiebel, D., Young, W., & Golap, K. 2007, in ASP Conf. Ser. 376, Astronomical Data Analysis Software and Systems XVI, ed. R. A. Shaw, F. Hill, & D. J. Bell (San Francisco, CA: ASP), 127

Mocanu, L. M., Crawford, T. M., Vieira, J. D., et al. 2013, ApJ, 779, 61

Narayanan, D., & Krumholz, M. R. 2017, MNRAS, 467, 50

Ouchi, M., Shimasaku, K., Furusawa, H., et al. 2010, ApJ, 723, 869

Papadopoulos, P. P., van der Werf, P. P., Xilouris, E. M., et al. 2012, MNRAS, 426, 2601

Pham, D. T., & Castellani, M. 2009, Proc. Inst. Mech. Eng., Part C: J. Mech. Eng. Sci., 223, 2919

Planck Collaboration, Ade, P. A. R., Aghanim, N., et al. 2016, A&A, 594, A13

Riechers, D. A., Bradford, C. M., Clements, D. L., et al. 2013, Natur, 496, 329

Rosenberg, M. J. F., van der Werf, P. P., Aalto, S., et al. 2015, ApJ, 801, 72

Scoville, N. 2003, JKAS, 36, 167

Spilker, J. S., Aravena, M., Marrone, D. P., et al. 2015, ApJ, 811, 124

Spilker, J. S., Marrone, D. P., Aravena, M., et al. 2016, ApJ, 826, 112

Stacey, G. J., Hailey-Dunsheath, S., Ferkinhoff, C., et al. 2010, ApJ, 724, 957

Stark, D. P. 2016, ARA&A, 54, 761

Strandet, M. L., Weiss, A., Vieira, J. D., et al. 2016, ApJ, 822, 80

Thompson, T. A., Quataert, E., & Murray, N. 2005, ApJ, 630, 167

Venemans, B. P., McMahon, R. G., Walter, F., et al. 2012, ApJL, 751, L25

Vieira, J. D., Marrone, D. P., Chapman, S. C., et al. 2013, Natur, 495, 344

Weiß, A., De Breuck, C., Marrone, D. P., et al. 2013, ApJ, 767, 88

Weiß, A., Downes, D., Henkel, C., & Walter, F. 2005, A&A, 429, L25

Weiß, A., Downes, D., Neri, R., et al. 2007, A&A, 467, 955